Impact of Reference-Layer Stray Field on the Write-Error Rate of Perpendicular Spin-Transfer-Torque Random-Access Memory

Arshid Nisar, Tanmoy Pramanik,* and Brajesh Kumar Kaushik†
Department of Electronics and Communication Engineering, Indian Institute of Technology Roorkee, Roorkee, Uttarakhand 247667, India

(Received 5 August 2022; revised 5 December 2022; accepted 12 January 2023; published 6 February 2023)

A finite-temperature micromagnetic study of magnetization switching and write-error rates in a perpendicular magnetic tunnel junction with and without synthetic antiferromagnetic layer (SAF) is presented. In the absence of SAF, magnetization switching is induced by domain-wall nucleation and propagation. Although the various modes of domain-wall propagation are observed to delay switching, it does not show an appreciable impact on the overall write-error-rate slopes. In the presence of the nonuniform stray field from the SAF assembly, the domain-wall-based switching modes turn on more complex magnetization dynamics that impedes the switching process. In cases where the SAF layers fail to balance each other contributing to a stronger stray field, incoherent switching modes give rise to metastable states with significantly longer lifetimes, and a dramatic change in the write-error slopes is observed. Simulation results are compared to recent experimental findings from time-domain measurements of spin-transfer-torque switching and measurements of anomalous write-error rates. These results directly prove the long-predicted relation of the SAF stray field to write-error anomaly in perpendicular spin-transfer-torque magnetic random-access memory and could be useful to solve the anomalous write-error problems.

DOI: 10.1103/PhysRevApplied.19.024016

I. INTRODUCTION

Spin-transfer-torque magnetic random access memory (STT MRAM) has emerged as one of the nonvolatile memory technologies that combine the benefits of fast access, unlimited endurance, high scalability, and easy integration with existing technology nodes [1–4]. The core component of STT MRAM is the magnetic tunnel junction (MTJ), composed of two ferromagnetic layers: reference layer (RL) and free layer (FL), separated by a thin oxide barrier. Magnetization of the RL is kept frozen with the help of a synthetic antiferromagnet (SAF) stack placed below the RL. Magnetization of the FL can be switched to parallel (P) or antiparallel (AP) with respect to the RL magnetization by the spin-transfer-torque (STT) effect. Thermal fluctuation at finite temperatures makes the magnetization process stochastic [5,6]. This randomness is reflected in the write process combined with other factors of uncertainty (e.g., process variation in geometrical and material parameter of the MTJ [7], variation in the driving transistors [8], backhopping at higher bias [9,10], self-heating effects [11,12]). Stray magnetic field from the SAF also impacts the write process and results in switching asymmetry between AP $\rightarrow$ P and P $\rightarrow$ AP transitions [13,14]. For larger size magnets, incoherent switching of various kinds, e.g., low-probability bifurcated switching [15], domain walls [16,17], etc., were observed to play a role. The probability that the FL fails to switch within a limited duration of write-pulse and write-current strength is termed as write-error rate (WER). The stochastic nature of the write process necessitates ultralow WER (of the order of 10^{-8} or lower) for practical memory design [2,5]. Experimentally it has been observed that the WER may not monotonically decrease with increasing write current or voltage as predicted by simple coherent rotation-based theory [6]. Increased write-error probabilities for shorter write-pulse time and intermediate ranges of write current and voltage have been reported. Such nonideal variations are referred to as anomalous WER or ballooning effect [1,2]. These nonideal effects are challenging for the applications where deterministic switching operation is sought. For feasible memory design, WER on the order of approximately 10^{-8} or below must be achieved within a short write time (approximately tens of nanoseconds) while keeping the write current at a minimum [2]. Previously anomalous increase of WERs has been attributed to incoherent switching within the FL magnet [1,2]. Stray field generated from the SAF was predicted to influence such modes [13,14]. Recent measurements of time-domain switching of perpendicular magnets have provided further insight into the switching modes for such devices [14,17,18]. Metastable states (also referred to as the intermediate

*pramanik.tanmoy@ece.iitr.ac.in
†bkk23fec@iitr.ac.in

states or medium states) have been observed to lock magnetization in intermediate resistance levels in between the P and AP states. Micromagnetic simulations at the zero temperature limit have been used to study domain-wall-mediated switching and impact of nonuniform stray field originating from the SAF. Asymmetric switching behavior between AP $\rightarrow$ P and P $\rightarrow$ AP transitions due to the nonuniformity in the stray field has been discussed by Volvach *et al*. [13] and Jiancheng *et al*. [19]. Bouquin *et al*. demonstrated that large-angle precession with domain wall and the nucleation of vertical Bloch lines at the center of the free layer result in temporal pinning effects and such domain-wall configurations behave as metastable states [17,18]. It is also predicted that such pinning effects can be eliminated if the Bloch and Néel wall profiles become degenerate in energy [18]. References [14,16,17] studied how the lateral size of the FL changes the switching process. It is observed that as the FL diameter is increased beyond approximately 50 nm, magnetization switching starts to deviate from coherent rotation model and domain-wall-based switching process takes over. For larger diameters (approximately 100 nm or higher), nonuniform modes become dominant. Presence of nonuniform stray field coupled with the domain-wall-based switching mode gives rise to more complex metastable states such as bubbles of the unswitched domain [14]. However, a direct relation of WER anomaly with the nonuniform magnetization states, such as domain-wall-based switching modes or SAF-induced metastable states, is yet to be clearly established.

In this work, a micromagnetic study of STT-induced switching of a perpendicular FL has been investigated at a finite temperature, with and without the stray field of the SAF stack. The behavior of P $\rightarrow$ AP and AP $\rightarrow$ P switching for varying stray-field profiles are presented. It is observed that the nonuniform stray field originating from an unoptimized SAF results in asymmetric switching, intermediate pinning, and write error. Finally, the effect of these nonuniform switching behaviors on WER as a function of write time and write voltages is discussed in detail.

II. SIMULATION DETAILS

Figures 1(a) and 1(b) show the MTJ stack considered in this work. Most of the results in this work are from a circular FL of diameter 120 nm. We deliberately choose such a large diameter as the incoherent switching modes easily form in magnets with larger dimension, consistent with earlier reports [13,14]. The dependency on the FL diameter is discussed at the end. Keeping the FL the same, we choose four different set of devices—we refer to them as "Standalone FL," "SAF I," "SAF II," and "SAF III" henceforth. For the "Standalone FL", we assume that the RL does not create any stray field on the FL and acts only as a spin polarizer for the STT effect. For the other three cases, we vary the SAF layer parameters to tailor the stray-field profiles, as shown in Figs. 1(c) and 1(d). Figure 1(c) shows the out-of-plane component of the magnetic field and Fig. 1(d) shows the in-plane component (along the radial direction) plotted with position along the FL diameter. The stray field follows the circular symmetry of the stack with more nonuniformity at the edge of the FL due to uncompensated moments. For "SAF I," we balance the SAF layers to minimize the average stray field on the FL [shown in Fig. 1(c)]. For "SAF II," we deliberately choose parameters such that a stronger stray field is created on the FL as compared to "SAF I" and the stray field favors the P state. For "SAF III," the parameters are again tweaked such that a stronger stray field is created on the FL favoring the AP state. At the center of the FL, "SAF I" configuration produces negligible stray field, whereas the "SAF II" configuration shows a positive field of approximately 100 Oe and the "SAF III" configuration shows a negative stray field of approximately 100–200 Oe along the out-of-plane z direction.

Following the magnetic orientation chosen for SAF layers and RL [Figs. 1(a) and 1(b)], FL magnetization switching from $+\hat{z}$ to $-\hat{z}$ corresponds to the P $\rightarrow$ AP transition. Conversely, $-\hat{z}$ to $+\hat{z}$ magnetization switching corresponds to the AP $\rightarrow$ P transition. The material parameters (typical of Co-Fe-B/MgO/Co-Fe-B material system [13]) and layer thicknesses chosen for the three cases are listed in Table I. We consider an exchange constant of 10 pJ/m for all the layers [20]. Micromagnetic simulations are carried out using one of the two publicly available solvers: OOMMF [21] or MUMAX3 [22]. The two solvers are benchmarked against each other to produce the same results. All the simulations are done using a discretization of $64 \times 64 \times 1$ cells and a fixed time step of 10 fs for the finite temperature integration using Heun's method. We simulate the switching at 233 K ($-40\,^{\circ}$C) to capture the finite-temperature effect while reducing the thermal randomness to some extent so that the nature of the incoherent excitations (e.g., Bloch wall versus Néel wall) are easily identified. Also, write-error issues originating from metastable states are usually known to be more pronounced at lower temperatures [23]. Effects of fieldlike torque, self-heating, and current-induced Oersted field are not included. Following Ref. [17], the critical switching voltage (V_{C0}) of the standalone FL is found to be approximately 0.2 V. We simulate switching events for varying voltages up to $6V_{C0}$.

To calculate the write-error rates, we simulate 10^3 trajectories for each case of applied voltage. The initial magnetization states are generated from a separate simulation where the FL magnetic moments are initialized to $\pm\hat{z}$ followed by a relaxation of 5 ns in the presence of thermal fluctuation field but without any STT term. For P $\rightarrow$ AP (or AP $\rightarrow$ P) switching, a trajectory is

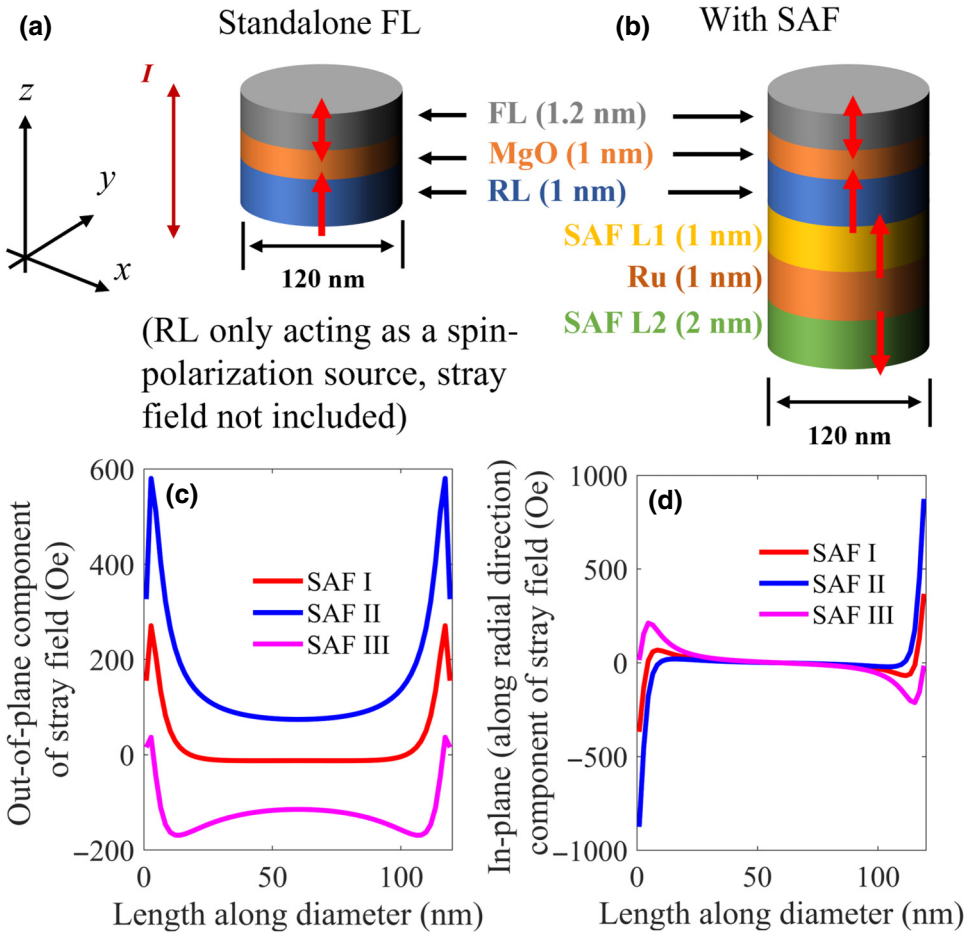

FIG. 1. Device structure, dimension, and layer thicknesses considered in this work. (a) Standalone FL—the RL is assumed to have no stray field on the FL and (b) MTJ stack with SAF layers included. Layer thicknesses are also marked. Other material parameters are listed in Table I. Three different SAF designs for (b) are considered—"SAF I," "SAF II," and "SAF III". For all three SAF configurations, the stray field inside the FL along the diameter is plotted in (c) and (d) for perpendicular and in-plane directions, respectively.

declared switched once it reaches below $m_z \leq -0.8$ (or $m_z \geq 0.8$) and never returns. Here, m_z should be understood as the space-averaged out-of-plane component of FL magnetization.

III. RESULTS AND DISCUSSION

Figure 2 summarizes the typical switching process for the standalone FL and the WER slopes for varying applied voltages. For the standalone FL, we discuss only the P $\rightarrow$ AP direction of switching since the switching process is completely symmetric between the AP $\rightarrow$ P and P $\rightarrow$ AP directions. Figures 2(a)–2(c) show a few different trajectories of magnetization switching at an applied voltage of $V = 3V_{C0}$, with the inset maps showing magnetization distribution at selected time instances (red dots on the trajectories). For a FL of such large dimension, domain-wall-based switching is expected. The domain wall nucleates at the edge of the FL (energetically favorable to form a reverse domain at the edge than in the center [24]). Following nucleation of the reverse domain, domain-wall propagation takes place. The majority of the trajectories are observed to sweep through the FL without stopping, like the one shown in Fig. 2(a). These trajectories would correspond to the experimentally measured conductance traces that show monotonic increase or decrease of conductance during switching [14,25]. We also observe trajectories that slow down when the domain wall is close to the center of the FL. Following the discussion in Ref. [18], we identify "central oscillation" like features in Fig. 2(b) and "multiple swing" like features in Fig. 2(c). Trajectories like Fig. 2(b) are observed when the domain wall crossing the center of the FL oscillates between a Néel and Bloch-like wall configuration. In Fig. 2(c), rotation of moments along the domain wall is observed to form a Bloch-line-like configuration that causes the domain wall to oscillate around the center multiple times delaying the

TABLE I. List of parameters.

Parameter		Value		
FL Saturation magnetization (M_s)		1.2×10^6 A/m		
FL Perpendicular anisotropy energy (K_u)		1×10^6 J/m^3		
SAF L2 Perpendicular anisotropy energy		1.24×10^6 J/m^3		
SAF L1 Perpendicular anisotropy energy		1.24×10^5 J/m^3		
RL perpendicular anisotropy energy		0.91×10^6 J/m^3		
Interlayer exchange coupling (between SAF L1 and L2)		-1.24×10^{-4} J/m^2		
Saturation magnetic moment		**SAF I**	**SAF II**	**SAF III**
	RL	0.8×10^6 A/m	1.1×10^6 A/m	0.6×10^6 A/m
	SAF L1	0.8×10^6 A/m	1.1×10^6 A/m	0.6×10^6 A/m
	SAF L2	0.6×10^6 A/m	0.4×10^6 A/m	0.8×10^6 A/m
Exchange stiffness (A_{ex})		10×10^{-12} J/m		
Gilbert-damping coefficient (α)		0.008		
Spin-polarization factor		0.6547		
Tunnel magnetoresistance ratio (TMR)		150%		
Temperature		−40 °C		
Discretization[a]		$64 \times 64 \times 1$ cells		

[a]Only FL is simulated, SAF stray field is calculated separately and added as an external magnetic field during STT-induced switching.

switching process. It is observed that the probability of the magnetization entering such states during switching depends on the applied voltage. We find that at $3V_{C0}$ the number of such cases is higher. At higher applied voltages, the switching is very fast and domain wall mostly follows the "ballistic" path as in Fig. 2(a). At lower voltages, the

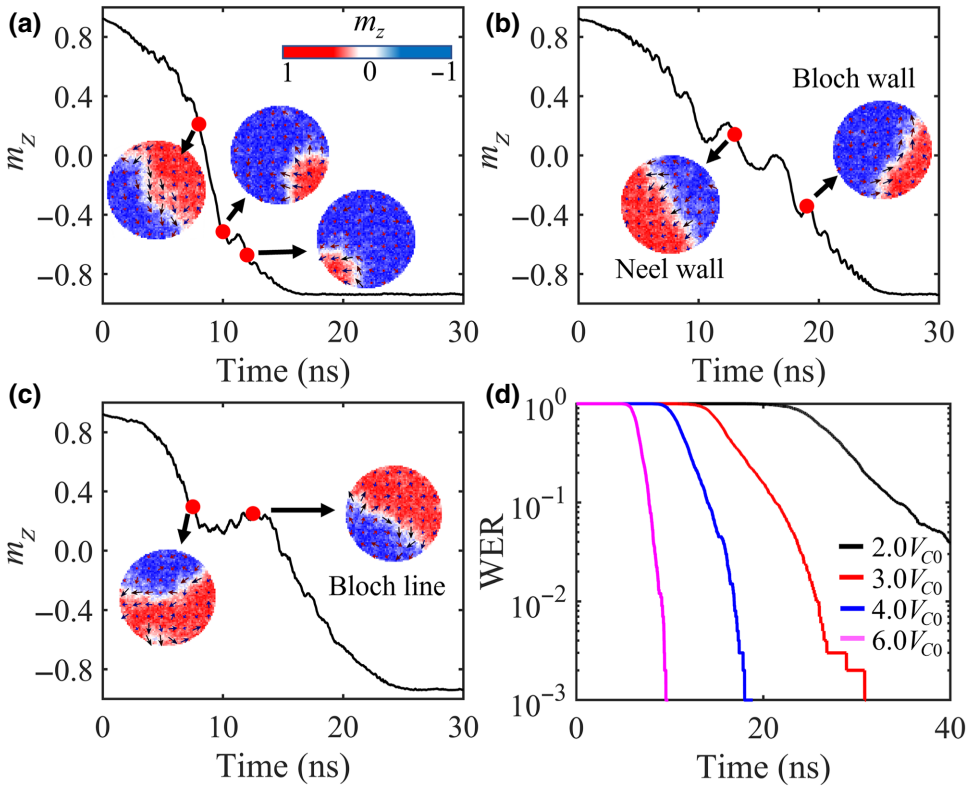

FIG. 2. (a)–(c) Typical switching processes observed for the standalone FL at $V = 3V_{C0}$. Domain-wall-mediated switching is observed in all cases. (a) Ballistic domain wall motion through the device achieving fast switching. (b) oscillatory and (c) multiple swing-like behaviors when the domain wall passes through the center of the FL. Inset in (a) shows the colormap used for the magnetization snapshots. (d) WER slopes calculated for varying applied voltages.

spin torque is presumably not strong enough to promote such high energy states. Over the simulated voltage range, none of the WER traces [Fig. 2(d)] show any clear change in the slopes as expected for anomalous ballooning of WER.

Now we turn to the case where the stray field from the SAF has been included in the simulations. Since the SAF stray field favors one of the states ($+\hat{z}$ or $-\hat{z}$), we calculate the WERs for both P → AP and AP → P transitions. Figure 3(a) shows the WER slopes for the different SAF configurations for a fixed applied voltage $V = 3V_{C0}$. Compared to the standalone FL case [black curve in Fig. 3(a)], the switching becomes asymmetric for SAF I to III. The stray field is very well optimized in SAF I as compared to SAF II or SAF III, therefore, the P → AP and AP → P transitions for SAF I follow the WER of the standalone FL closely, with a small difference in slopes due to the positive out-of-plane stray field at the edge of the FL favoring the P state. Few metastable states are observed for both P → AP and AP → P transitions that last for a relatively short duration of time. On the other hand, the positive out-of-plane stray-field distribution for SAF II strongly favors the P state, hence the WER slopes are much steeper (faster switching) for AP → P transition. Conversely, the P → AP transition for SAF II show shallower WER slope (slower switching). For SAF III, P → AP transition is faster aided by an overall negative out-of-plane stray field favoring the AP state. The SAF III AP → P transition shows a similar nature as the SAF II P → AP transition with a drastic change in the WER slope appearing after approximately 30 ns. For both cases, WER remains very high even after 60 ns where we stop the simulations. Such changes of slope in the WER could be related to the anomalous ballooning effect. The difficulty in comparing the simulations with the experimental observations is that the WER is usually measured in the experiments as a function of write voltage while keeping pulse width the same. To better mimic the experimental data, we also estimate the WER for a fixed pulse width of 30 ns while varying the write voltages. The result is shown in Fig. 3(b). (For these simulations, the write voltage is applied for a duration of 30 ns and then turned off. The simulations are continued for another 30 ns without the STT term to relax the magnetic state to either P or AP configuration. The WER is then estimated from the final magnetization states. The WER estimated in this manner also includes the impact of backflipping due to the metastable states as explained in the following discussion). Figure 3(b) also shows a change of slope in the WER curve for SAF II P → AP and SAF III AP → P transitions. No such feature is visible for the standalone FL and SAF I. The behavior of WER for SAF II P → AP transition (and SAF III AP → P transition) in Fig. 3(b) now resembles the ballooning effect of WER reported in experiments [2,10].

A change of slope in the WER curve can be explained in terms of metastable states that adds random delay time by trapping the magnetization during the switching from one global minimum to the other [18]. To get a deeper insight into the origin of metastable states and the ballooninglike effects observed here, we look for trajectories that remain unswitched for relatively longer time (contributes to the WER tail). Figure 4 summarizes a few such example trajectories observed in the simulations. For

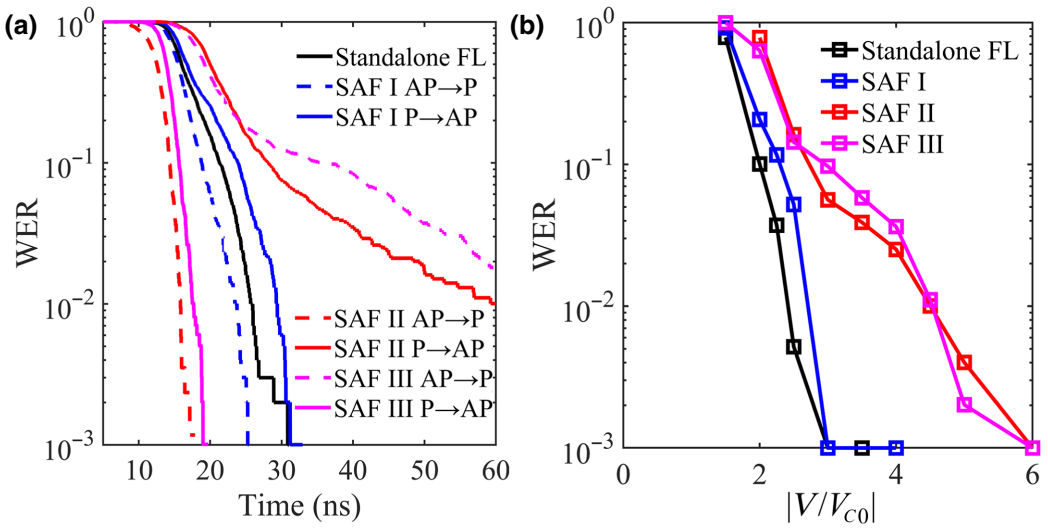

FIG. 3. (a) WER slopes at $V = 3V_{C0}$ showing the impact of SAF-induced stray field. Compared to standalone FL, one of the switching directions is aided and the other direction is hindered by the stray field. The WER slopes change dramatically for the SAF II P → AP switching and SAF III AP → P switching configurations as the metastable oscillatory states prevail for these two configurations. (b) WER plotted versus normalized write voltage for selected cases. SAF II P → AP and SAF III AP → P switching show distinct plateau in the WER tails—similar to the ballooning effect reported in experimental studies.

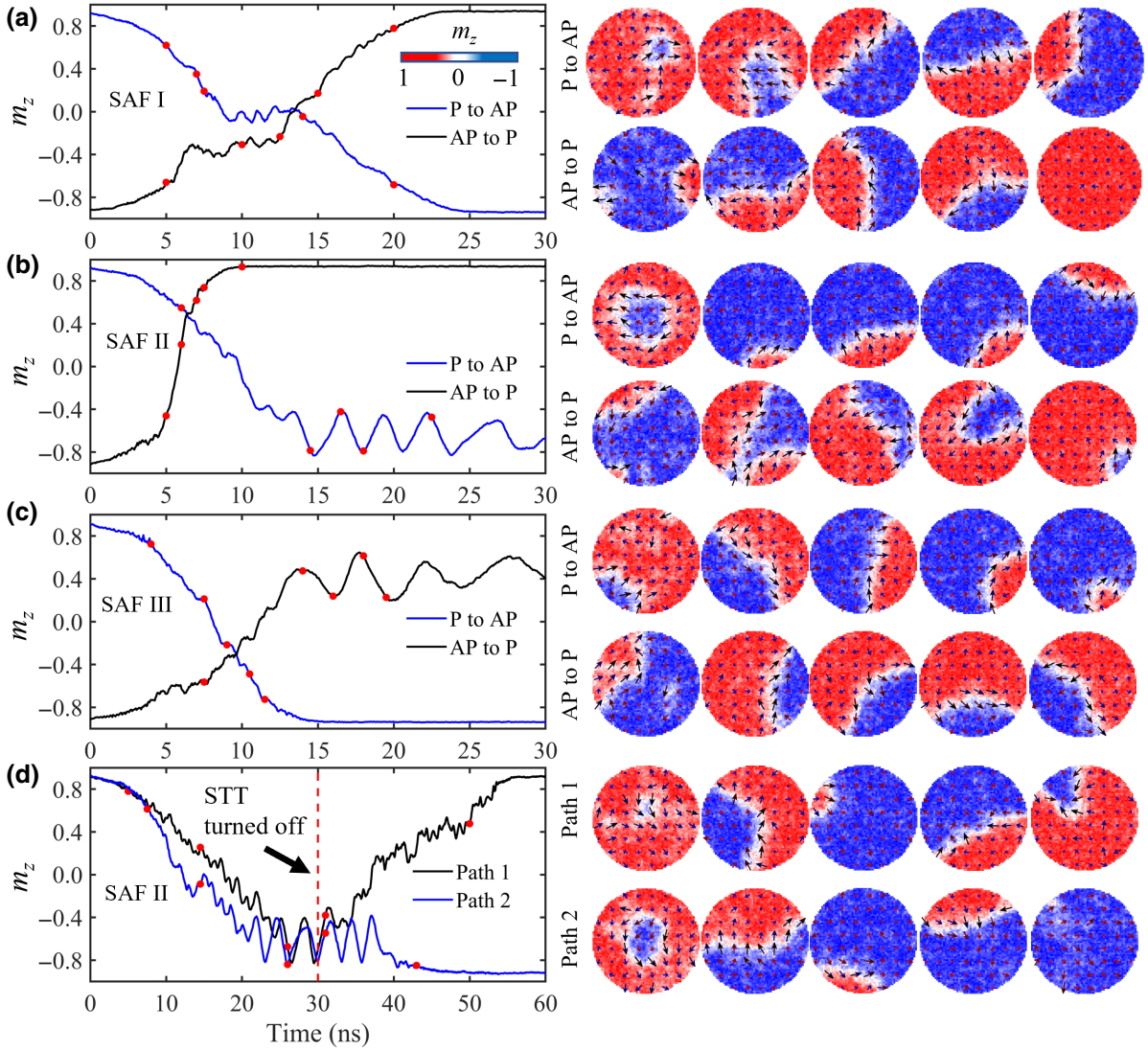

FIG. 4. Typical switching events and metastable states for varying SAF configurations—(a) for SAF I, P → AP switching starts by a nucleation of a reversed domain at the center followed by domain-wall motion as in standalone FL. AP → P starts by edge nucleation; (b) for SAF II with stronger stray fields, P → AP switching is hindered by the oscillation of unswitched bubble around the edges while AP → P switching becomes mostly ballistic aided by the stray field; (c) for SAF III, nucleation of reverse domain starts from the edge for both direction of switching, but the AP → P direction now shows similar metastable states as in P → AP direction for SAF II. (d) Trapped bubble of unswitched domain evolves during P → AP switching in SAF II. After the write pulse is turned off at 30 ns, the FL may return to initial state (path 1) or switch to the desired state (path 2) causing increased write-error rates. Magnetization snapshots are shown on the right corresponding to the time instants marked by the red dots. Inset in (a) shows the colormap used for the magnetization snapshots.

each case in Figs. 4(a)–4(d), the magnetization snapshots at the time instants marked by red dots are shown on the right. Figure 4(a) shows two trajectories for P → AP and AP → P transitions, respectively, for SAF I. As compared to standalone FL where edge nucleation is preferred, for SAF I P → AP transition, we also find instances of center nucleation. After nucleation, the reverse domain then moves to the edge of the FL creating a domain wall that is further pushed through the FL to complete the switching process. The AP → P transitions for SAF I are initiated by edge nucleation very easily and then completed by domain-wall motion. Domain-wall propagation again found to follow one of the three types of paths as described in Fig. 2 for the standalone FL. SAF II P → AP transition follows similar nucleation process as in SAF I [Fig. 4(b)], except that the central nucleation process now is preferred over edge nucleation. In addition, the domain-wall propagation is hampered by the strong stray field at the edge (favoring P state) and small unswitched domains [red colored domain in Fig. 4(b) P → AP snapshots] are

found trapped for a longer instance. Such unswitched trapped domains behave as metastable states and they are observed to randomly escape out of this oscillatory motion to complete the switching. We believe these are the same "bubble" states as observed previously in Ref. [14]. The conductance of such states could be quite close to the P or AP states. The AP → P transitions for SAF II [Fig. 2(b) black trajectory], on the other hand, are initiated by edge nucleation and then completed by fast domain-wall propagation. For SAF III, we mostly observe edge nucleation for both transitions followed by domain-wall propagation [Fig. 4(c)]. However, for AP → P transition, we find that unswitched $-\hat{z}$-magnetized domains now remain trapped and cause delay. In Fig. 4(d) we show how these oscillatory metastable states (bubbles of unswitched domain) can cause increased WER by flipping back to the SAF-favored state. After the current pulse is turned off at 30 ns, the bubble is either pushed out (path 2, blue trajectory) or it expands taking the FL back to the initial state (path 1, black trajectory). SAF III AP → P transitions are also found to behave similarly (not shown). It is now evident that these SAF-induced metastable states are responsible for the increased WER in Fig. 3(b).

The differences in the nucleation and propagation of reverse domain during switching for the three cases of SAF can be understood from the out-of-plane stray-field distributions in Fig. 1(c). The center nucleation in SAF I and SAF II is caused by the very strong out-of-plane stray fields at the edge, approximately 300 and approximately 600 Oe for SAF I and SAF II, respectively. This positive field (favoring P state) opposes the edge nucleation during P → AP transition and forces center nucleation. SAF III, has a much weaker positive field peak at the edge (approximately 20 Oe), which is not strong enough to win over the energy benefits of edge nucleation explaining why SAF III does not show any center nucleation. In the case of SAF II, the out-of-plane stray field strength is approximately 100 Oe near the device center and it is very strong

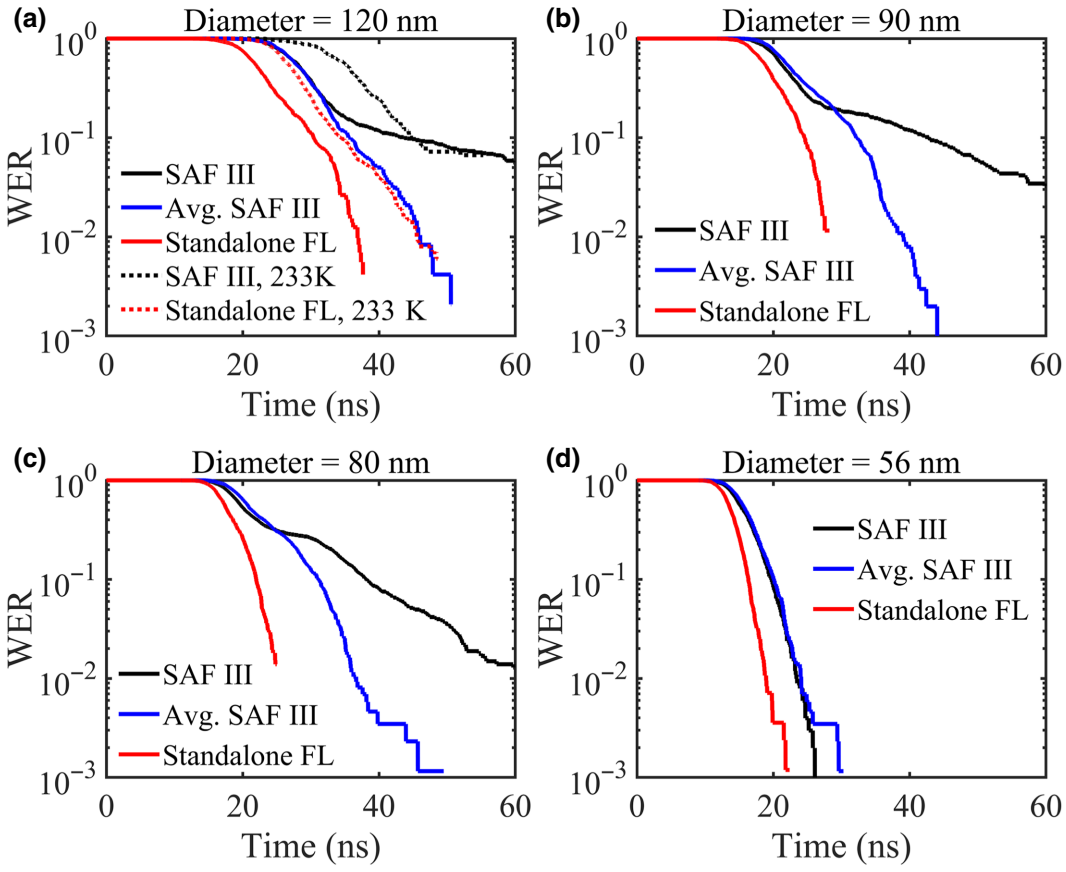

FIG. 5. Impact of SAF-induced stray field on the WER slopes for varying FL diameter: (a) 120, (b) 90, (c) 80, and (d) 56 nm. For each case the WER slope of standalone FL (red) and WER including SAF III (black) is plotted. Additionally, WER slopes including an average SAF field (blue) is also plotted for comparison. At 56 nm, the effect of SAF is the same as the average out-of-plane field. For larger diameter, SAF field causes additional features. All simulations are done for 300 K. The temperature dependence of WER is shown in (a) for the 120-nm device with 233 K (dotted lines) and 300 K (solid lines) simulation results. Higher temperature lowers WER. The same SAF parameters (Table I) are used for all, except the diameter. Applied voltage is twice the critical voltage for each diameter.

(approximately 600 Oe) at the edges. This nonuniformity in the field hinders the domain-wall propagation during the P → AP transition and results in the metastable bubble domains with oscillatory response as shown in Fig. 4(b). The domain-wall propagation during the AP → P transition is favored by the overall positive field and results in smooth switching. In contrast, for SAF III, since the AP state is preferred, the domain-wall propagation during AP → P transition is opposed while it crosses the FL (the peak negative field next to the edge acts as a trap for the bubble domain), again resulting in the oscillatory response as observed in Fig. 4(c).

Finally, in Fig. 5 we comment on the dependence of the WER on FL diameter and temperature. Figure 5 shows the WER slopes for FL diameters of 56, 80, 90, and 120 nm at 300 K for an applied voltage of twice the critical voltage for each diameter. For each diameter, three different WER slopes are calculated—standalone FL (red line), SAF III (black line), and a test case (blue line). The test cases are simulated by including an effective magnetic field (uniform across the FL) given by the space-averaged out-of-plane component of the SAF III stray field. Figure 5(a) shows the WER slopes for the 120-nm FL at 233 and 300 K. We note that the temperature increase reduces the overall WER as expected [26,27], but the behavior of the SAF-induced metastable states remains the same. For this small change in temperature, we ignore any variation in the material parameters. A larger variation in temperature (due to self-heating or high-temperature operation) could be studied in the future with temperature dependence of the material parameters included in the simulations. The impact of metastable states remains clearly visible down to a diameter of 80 nm [Fig. 5(c)]. Comparing the blue (average stray field) and black lines (SAF III field) in Figs. 5(a)–5(c) during early phases of switching, it is observed that the WER slopes including SAF III follows the slopes obtained from simulations with the average stray field. However, for diameter of 80 nm and above, the behavior of the SAF III WER tail is markedly different indicating the appearance of the metastable states that impact the switching rate. With the diameter decreasing from 120 to 80 nm, the slope of the SAF III WER tail improves (faster switching) and moves closer to the slope obtained for the average field. Decreasing the impact of the SAF stray field indicates progressively weaker metastable states as the FL diameter is reduced. At 56 nm [Fig. 5(d)], the impact of the SAF III field appears to be the same as the average stray magnetic field—the additional changes in WER slope due to metastable states do not appear. The switching process for 56 nm is observed to be quasicoherent for some trajectories and smooth (ballistic) domain-wall motion for others. At 30-nm diameter (not shown), the switching process becomes quasiuniform. Clear domain-wall formation is observed when the diameter is increased to 80 nm. The change in behavior with increasing diameter agrees with previous reports [13,14,17,25,28]. Table II summarizes the crossover diameters for quasiuniform to domain-wall-based switching and the appearance of metastable states as observed in experiments and simulations. Exchange lengths (l_{ex}) are also noted in Table II to provide a more meaningful comparison since the material parameters are different across each of these studies. Overall, we find that the domain-wall-mediated switching takes over at approximately $5l_{ex}$ and the metastable states with significant lifetimes start to appear at approximately $10l_{ex}$.

TABLE II. Diameter dependence of the switching mechanisms.

Reference	Crossover from quasiuniform to domain-wall-based switching	Appearance of metastable states	Exchange length (l_{ex})
[13]	∼30 nm	∼80 nm	7.4 nm
[14]	∼50–80 nm	∼150 nm	–
[17,25]	∼22–25 nm	∼60 nm	4.8 nm
[28]	<30 nm	–	4.5 nm
This work	∼30–56 nm	∼80 nm	10.3 nm

IV. CONCLUSION

In summary, we demonstrate a direct relation of the WER ballooning to the SAF-induced stray field using finite-temperature micromagnetic simulation of STT switching of a perpendicular STT-RAM cell. We observe various modes of domain-wall switching consistent with previous experimental and theoretical reports. We find that these modes do not show an appreciable change in the WER slope adequate to explain the ballooning effect. However, once the SAF-induced stray field is taken into consideration, the nucleation (to initiate the switching) and annihilation (to complete the switching) of domains could be severely impacted due to the edge nonuniformity of the stray field. Specifically, we show that the bubbles of the unswitched domain can remain trapped around the edge of the free layer and cause the free layer to flip back to the initial state once the switching current or voltage is turned off. The increase in WER due to these metastable states could explain the ballooning effect observed in the experiments. Optimizing the SAF balance and minimizing the stray field would help to avoid such metastable states and ballooning effects.

ACKNOWLEDGMENT

Authors would like to acknowledge the Supercomputing facility of IIT Roorkee established under National Supercomputing Mission (NSM), Government of India and supported by Centre for Development of Advanced Computing (CDAC), Pune, for proving high-performance

computing resources. T.P. thanks Dr U. Roy for careful reading of the manuscript and feedback on the results. T.P. and B.K.K. acknowledge support from the Science and Engineering Research Board, Govt. of India, Grant No. SRG/2021/000377 and Grant No. CRG/2019/004551, respectively.

[1] O. Golonzka, J.-G. Alzate, U. Arslan, M. Bohr, P. Bai, J. Brockman, B. Buford, C. Connor, N. Das, B. Doyle *et al.*, in *2018 IEEE International Electron Devices Meeting (IEDM)* (IEEE, San Francisco, CA, 2018), pp. 18.1.1–18.1.4.

[2] J. G. Alzate, U. Arslan, P. Bai, J. Brockman, Y. J. Chen, N. Das, K. Fischer, T. Ghani, P. Heil, P. Hentges *et al.*, in *2019 IEEE International Electron Devices Meeting (IEDM)* (IEEE, San Francisco, CA, USA, 2019), pp. 2.4.1–2.4.4.

[3] C.-H. Chen, C.-Y. Chang, C.-H. Weng, T.-H. Kuo, C.-Y. Wang, M.-C. Shih, T.-W. Chiang, Y.-J. Lee, R. Wang, K.-H. Shen *et al.*, in *16 nm FinFET CMOS Process, Symposium on VLSI Technology Digest of Technical Papers 2* (2021).

[4] V. B. Naik, K. Yamane, T. Y. Lee, J. Kwon, R. Chao, J. H. Lim, N. L. Chung, B. Behin-Aein, L. Y. Hau, D. Zeng, *et al.*, in *2020 IEEE International Electron Devices Meeting (IEDM)* (2020), pp. 11.3.1–11.3.4.

[5] A. V. Khvalkovskiy, D. Apalkov, S. Watts, R. Chepulskii, R. S. Beach, A. Ong, X. Tang, A. Driskill-Smith, W. H. Butler, P. B. Visscher, *et al.*, Basic principles of STT-MRAM cell operation in memory arrays, J. Phys. D: Appl. Phys. **46**, 074001 (2013).

[6] W. H. Butler, T. Mewes, C. K. A. Mewes, P. B. Visscher, W. H. Rippard, S. E. Russek, and R. Heindl, Switching distributions for perpendicular spin-torque devices within the macrospin approximation, IEEE Trans. Magn. **48**, 4684 (2012).

[7] U. Roy, T. Pramanik, S. Roy, A. Chatterjee, L. F. Register, and S. K. Banerjee, Machine learning for statistical modeling: the case of perpendicular spin-transfer-torque random access memory, ACM Trans. Des. Autom. Electron. Syst. **26**, 1 (2021).

[8] Y. Zhang, X. Wang, H. Li, and Y. Chen, STT-RAM cell optimization considering MTJ and CMOS variations, IEEE Trans. Magn. **47**, 2962 (2011).

[9] T. Devolder, O. Bultynck, P. Bouquin, V. D. Nguyen, S. Rao, D. Wan, B. Sorée, I. P. Radu, G. S. Kar, and S. Couet, Back hopping in spin transfer torque switching of perpendicularly magnetized tunnel junctions, Phys. Rev. B **102**, 184406 (2020).

[10] J. Z. Sun and C. Safranski, Metrology and metrics for spin-transfer-torque switched magnetic tunnel junctions in memory applications, J. Magn. Magn. Mater. **563**, 169878 (2022).

[11] S. Van Beek, B. J. O'Sullivan, P. J. Roussel, R. Degraeve, E. Bury, J. Swerts, S. Couet, L. Souriau, S. Kundu, S. Rao *et al.*, in *2018 IEEE International Electron Devices Meeting (IEDM)* (2018), pp. 25.2.1–25.2.4.

[12] J. J. Kan, C. Park, C. Ching, J. Ahn, L. Xue, R. Wang, A. Kontos, S. Liang, M. Bangar, H. Chen *et al.*, in *2016 IEEE International Electron Devices Meeting (IEDM)* (2016), pp. 27.4.1–27.4.4.

[13] I. Volvach, J. G. Alzate, Y.-J. Chen, A. J. Smith, D. L. Kencke, and V. Lomakin, Thermal stability and magnetization switching in perpendicular magnetic tunnel junctions, Appl. Phys. Lett. **116**, 192408 (2020).

[14] T. Devolder, A. Le Goff, and V. Nikitin, Size dependence of nanosecond-scale spin-torque switching in perpendicularly magnetized tunnel junctions, Phys. Rev. B **93**, 224432 (2016).

[15] T. Min, Q. Chen, R. Beach, G. Jan, C. Horng, W. Kula, T. Torng, R. Tong, T. Zhong, D. Tang, *et al.*, A study of write margin of spin torque transfer magnetic random access memory technology, IEEE Trans. Magn. **46**, 2322 (2010).

[16] A. Meo, S. Sampan-a-pai, P. B. Visscher, R. Chepulskyy, D. Apalkov, J. Chureemart, P. Chureemart, R. W. Chantrell, and R. F. L. Evans, Spin transfer torque switching dynamics in CoFeB/MgO magnetic tunnel junctions, Phys. Rev. B **103**, 054426 (2021).

[17] P. Bouquin, S. Rao, G. S. Kar, and T. Devolder, Size dependence of spin-torque switching in perpendicular magnetic tunnel junctions, Appl. Phys. Lett. **113**, 222408 (2018).

[18] P. Bouquin, J.-V. Kim, O. Bultynck, S. Rao, S. Couet, G. S. Kar, and T. Devolder, Stochastic Processes in Magnetization Reversal Involving Domain-Wall Motion in Magnetic Memory Elements, Phys. Rev. Appl. **15**, 024037 (2021).

[19] H. Jiancheng, S. C. Hin, V. B. Naik, M. Tran, L. S. Ter, and H. Guchang, Effect of the stray field profile on the switching characteristics of the free layer in a perpendicular magnetic tunnel junction, J. Appl. Phys. **117**, 17B721 (2015).

[20] M. Yamanouchi, A. Jander, P. Dhagat, S. Ikeda, F. Matsukura, and H. Ohno, Domain structure in CoFeB thin films with perpendicular magnetic anisotropy, IEEE Magn. Lett. **2**, 3000304 (2011).

[21] M. J. Donahue and D. G. Porter, OOMMF User's Guide, Version 1.2 A3, Interagency Report NISTIR 6376, (2002).

[22] The Design and Verification of MuMax3: AIP Advances: Vol 4, No 10, https://aip.scitation.org/doi/10.1063%2F1.4899186

[23] S. Gao, B. Chen, and Y. Zhao, Systematic study of medium states in spin-transfer torque magnetoresistance random access memory and their implication for the bit error rate, IEEE Electron Device Lett. **41**, 557 (2020).

[24] G. D. Chaves-O'Flynn, G. Wolf, J. Z. Sun, and A. D. Kent, Thermal Stability of Magnetic States in Circular Thin-Film Nanomagnets with Large Perpendicular Magnetic Anisotropy, Phys. Rev. Appl. **4**, 024010 (2015).

[25] P. Bouquin, J.-V. Kim, O. Bultynck, S. Rao, S. Couet, G. S. Kar, and T. Devolder, Spin-torque induced wall motion in perpendicularly magnetized discs: ballistic versus oscillatory behavior, Phys. Rev. B **103**, 224431 (2021).

[26] L. Lang, Y. Jiang, F. Lu, C. Wang, Y. Chen, A. D. Kent, and L. Ye, A low temperature functioning CoFeB/MgO-based perpendicular magnetic tunnel junction for cryogenic

nonvolatile random access memory, Appl. Phys. Lett. **116**, 022409 (2020).

[27] L. Rehm, G. Wolf, B. Kardasz, M. Pinarbasi, and A. D. Kent, Sub-nanosecond spin-torque switching of perpendicular magnetic tunnel junction nanopillars at cryogenic temperatures, Appl. Phys. Lett. **115**, 182404 (2019).

[28] C. Yoshida, T. Tanaka, T. Ataka, J. Fujisaki, K. Shimizu, T. Hirahara, H. Shitara, A. Furuya, and Y. Uehara, Size dependence of the thermal stability factor in a perpendicular CoFeB/MgO magnetic tunnel junction studied by micromagnetic simulations, Jpn. J. Appl. Phys. **58**, SBBB05 (2019).